CrossMark

CARDIAC

Four-dimensional flow MRI for evaluation of post-stenotic turbulent flow in a phantom: comparison with flowmeter and computational fluid dynamics

Jihoon Kweon[1] · Dong Hyun Yang[2] · Guk Bae Kim[2] · Namkug Kim[2] ·
MunYoung Paek[3] · Aurelien F. Stalder[4] · Andreas Greiser[4] · Young-Hak Kim[1]

Abstract
Objectives To validate 4D flow MRI in a flow phantom using a flowmeter and computational fluid dynamics (CFD) as reference.
Methods Validation of 4D flow MRI was performed using flow phantoms with 75 % and 90 % stenosis. The effect of spatial resolution on flow rate, peak velocity and flow patterns was investigated in coronal and axial scans. The accuracy of flow rate with 4D flow MRI was evaluated using a flowmeter as reference, and the peak velocity and flow patterns obtained were compared with CFD analysis results.
Results 4D flow MRI accurately measured the flow rate in proximal and distal regions of the stenosis (percent error ≤3.6 % in axial scanning with 1.6-mm resolution). The peak velocity of 4D flow MRI was underestimated by more than 22.8 %, especially from the second half of the stenosis. With 1-mm isotropic resolution, the maximum thickness of the recirculating flow region was estimated within a 1-mm difference, but the turbulent velocity fluctuations mostly disappeared in the post-stenotic region.

Conclusion 4D flow MRI accurately measures the flow rates in the proximal and distal regions of a stenosis in axial scan but has limitations in its estimation of peak velocity and turbulent characteristics.
Key points
• *4D flow MRI accurately measures the flow rate in axial scan.*
• *The peak velocity was underestimated by 4D flow MRI.*
• *4D flow MRI demonstrates the principal pattern of post-stenotic flow.*

Keywords 4D flow MRI · Pathological constriction · Dimensional measurement accuracy · Computational fluid dynamics

Abbreviations
CFD   Computational fluid dynamics
PC-MRI Phase contrast magnetic resonance imaging
SNR   Signal-to-noise ratio

✉ Dong Hyun Yang
donghyun.yang@gmail.com

[1] Department of Cardiology and Heart Institute, Asan Medical Center, University of Ulsan College of Medicine, Seoul, South Korea

[2] Department of Radiology and Research Institute of Radiology, Cardiac Imaging Center, Asan Medical Center, University of Ulsan College of Medicine, Asanbyeongwon-gil 86, Seoul 138-736, South Korea

[3] Siemens Healthcare, Seoul, Korea

[4] Siemens Healthcare, Erlangen, Germany

Introduction

Time-resolved, three-dimensional (3D) phase contrast magnetic resonance imaging (PC-MRI), termed '4D flow MRI', allows visualisation of 3D flow structures with a single scan. It has been used to identify the blood-flow characteristics of the thoracic aorta [1, 2], pulmonary arteries [3–5] and carotid arteries [6], and has provided an insight into global and local circulation of blood flow. In addition, a quantitative parameter measured by four-dimensional (4D) flow MRI in the main pulmonary artery, vortex duration, is useful for predicting the severity of pulmonary hypertension [3].

There have been many attempts to assess the measurement accuracy and clinical feasibility of 4D flow MRI by

comparing flow parameters. Evaluation of the flow rate using 4D flow MRI has exhibited an accuracy comparable to that of two-dimensional (2D) flow MRI [7, 8]. Peak velocity measured with 4D flow MRI is underestimated compared with that of Doppler ultrasound [9, 10]. In a recent experimental study using a flow phantom, the flow field from 4D flow MRI was highly consistent with that of computational fluid dynamics (CFD) and particle image velocimetry [11].

Nonetheless, the quantitative accuracy of 4D flow MRI remains to be fully evaluated. In particular, although spatial resolution and scanning orientation have dominant effects on scan time and artefacts [12], previous studies considered narrow variations in spatial resolution [2] or only made comparisons with clinical measures such as 2D flow MRI [13]. Therefore, the purpose of our present study was threefold: (1) to quantify the accuracy of 4D flow MRI in measuring flow rate across severe stenosis using a flowmeter; (2) to investigate the effect of the spatial resolution on the peak velocity measurement; (3) and to assess the flow patterns of 4D flow MRI by comparing them with CFD analysis.

## Methods

Flow phantom preparation

Two flow phantoms were constructed to simulate turbulent stenotic flow. Stenosis was modelled as rigid circular pipes with a 22-mm internal diameter (Fig. 1), and the phantoms were fabricated with a 3D printer (Projet 3510 SD; 3D Systems, Rock Hill, SC, USA). Stenosis models of 75 % and 90 % area constrictions were considered with the shape of a sinusoidal function [14], and the cross-sectional areas at the narrowest region were 95 mm² and 38 mm², respectively. The stenosis was situated at the centre of the scanner bore and the longitudinal axis of the stenosis model, that is, the flow direction was parallel to the magnetic field.

A non-pulsatile flow of blood-equivalent fluid (Hextend; CJ Corp., Seoul, Korea) from an output-adjustable pump (Eheim Compact Plus 5000; Eheim, Deizisau, Germany) entered the inlet of the stenosis phantom. The flow rates for the 90 % and 75 % stenosis phantoms were controlled as 5.4 and 14.7 L/min, respectively, to match the average velocity at the stenosis, and an electromagnetic flowmeter (VN20; Aichi Tokei Denki, Nagoya, Japan) provided the flow rate as a reference. The components of the flow circuit were connected via silicon tubing, and devices suspected of affecting the data acquisition were kept out of the MR room.

Magnetic resonance imaging (MRI)

Image acquisition of the turbulent stenotic flow was performed on a 3 T scanner (MAGNETOM Skyra; Siemens Healthcare, Erlangen, Germany) using an 18-channel body matrix coil. A gradient-echo sequence was used for conventional PC-MRI provided by Siemens (linear phase-encoding scheme) and the GRAPPA (generalised auto-calibrating partially parallel acquisition) factor was two. The acquisition parameters are summarised in Table 1. In 4D flow MRI, the spatial resolutions in coronal and axial scanning orientations were varied to investigate their effects on the flow measurement. The coronal and axial scanning directions were parallel and perpendicular to the flow direction, respectively. The number of acquired data points with a fixed volumetric field of view is inversely proportional to the voxel size. For example, with the finest spatial resolution considered ($1 \times 1 \times 1$ mm³), approximately 380 data points per axial plane
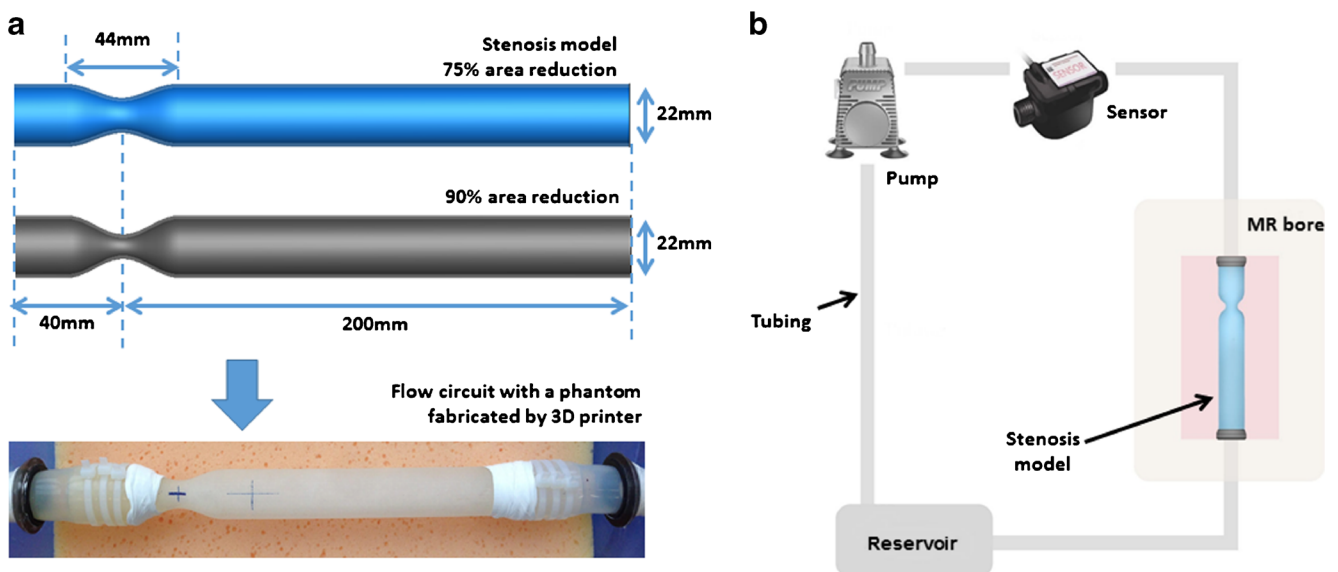
Fig. 1 (a) Geometry of the stenosis phantom and procedures for constructing the flow circuit. (b) Schematic diagram of the flow circuit

Table 1 Magnetic resonance imaging (MRI) acquisition parameters

	4D flow MRI				2D flow MRI	
	75 % stenosis		90 % stenosis		75 % stenosis	90 % stenosis
Scanning orientation	Coronal	Axial	Coronal	Axial	Axial	Axial
Spatial resolution, mm	3.0 / 1.6 / 1.0 (isotropic)	3.0 / 1.6 (isotropic)	3.0 / 1.6 / 1.0 (isotropic)	3.0 / 1.6 (isotropic)	1.6	0.6
Repetition time, ms	71.0 / 75.5 / 79.4	68.3 / 73.2	71.8 / 75.5 / 79.6	67.8 / 73.0	22.7	22.9
Echo time†, ms	4.47 / 4.77 / 4.93	4.14 / 4.48	4.59 / 4.78 / 4.94	4.08 / 4.47	3.1	3.1
Number of time frames	12 / 11 / 11	13 / 12	10 / 9 / 9	10 /10	43	32
Field of view*, mm	$290 \times 290 \times 36$	$290 \times 146 \times 96$	$192 \times 192 \times 30$	$192 \times 168 \times 108$	72×50	72×50
Scan time, s	187 / 465 / 1,028	529 / 1,303	101 / 237 / 565	271 / 681	13	20
Velocity-encoding range, cm/s	350	350	400	400	350	400
Flip angle, degree	10	10	10	10	30	30
Bandwidth, Hz/pixel	200	200	200	200	392	392

†Echo time and repetition time are set to the minimum in each acquisition

*Field of view is adjusted according to the spatial resolution

were achieved in the flow area of the normal region, whereas with 3-mm isotropic resolution, approximately 42 points per axial plane were obtained in the flow area. The velocity-encoding range was set to the minimum value so that aliasing did not occur in the narrowest region. Axial plane images of 2D flow MRI were obtained for comparison with those of 4D flow MRI, as shown in Fig. 2. For 75 % stenosis, a spatial resolution of 1.6×1.6 mm^2 was compared with the 4D flow MRI result of the same in-plane resolution, and for 90 % stenosis, the data set was measured with a resolution of 0.6×0.6 mm^2 to resolve the flow at the narrowest region (diameter = 6.96 mm).

The flow rate at each time point was calculated using a semi-automatic detection of the flow area in a prototype investigational software, 4D Flow (Siemens Healthcare) and

CVI software (Circle Cardiovascular Imaging Inc., Canada) for 4D and 2D flow MRI, respectively (Table 2). Four-dimensional flow also provided streamlines in a flow area for visualisation (Fig. 6). For a statistical analysis of the peak velocity and a visualisation of the flow field, the velocity in space and time was extracted using a customised MATLAB-based software (MathWorks, Natick, MA, USA).

Computational fluid dynamics

To investigate turbulent flow in the stenosis model, a large eddy simulation with a dynamic Vreman model was conducted [15] and an immersed boundary method for incompressible flow was used to identify the stenosis in a cylindrical
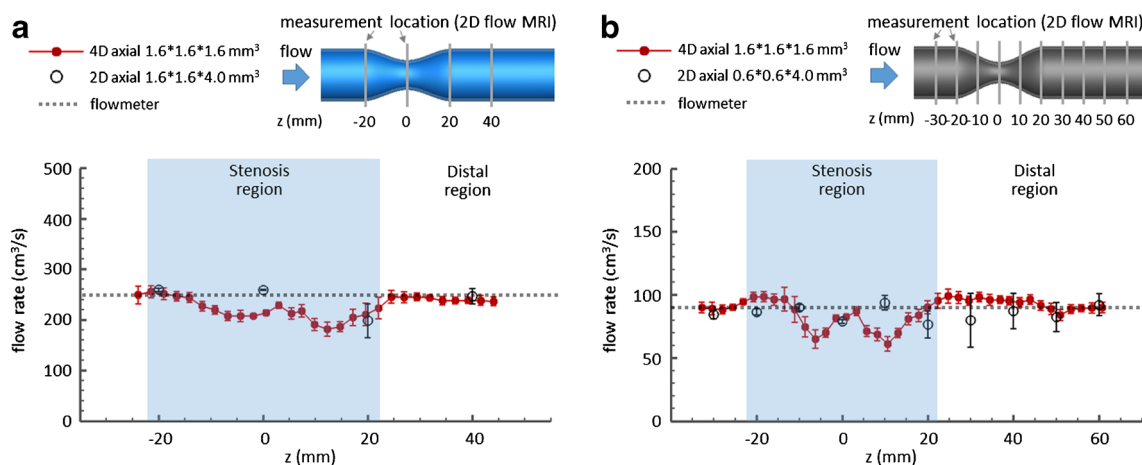
Fig. 2 Spatial variations in the time-averaged flow rate measured with 4D flow magnetic resonance imaging (MRI) for (**a**) 75 % and (**b**) 90 % stenosis. The results of 2D flow MRI under the same flow conditions are also shown, and the corresponding imaging planes are illustrated in the top part of the image. A blue-shaded box denotes the stenosis region. The error bar signifies the temporal standard deviation at each location and, as a reference, the flow rate measured using the flowmeter is marked as straight dashed gray lines. The flow rate of computational fluid dynamics (CFD) analysis is the same as the 2D flow MRI measurement at the phantom inlet, resulting in an almost identical value as that of the flowmeter

Table 2 Percent error of flow rate measured by 4D flow magnetic resonance imaging (MRI) according to scan direction, spatial resolution and velocity-encoding range

Scan direction	Spatial resolution, mm	75 % stenosis (velocity-encoding range = 350 cm/s)			90 % stenosis (velocity-encoding range = 400 cm/s)		
		Proximal	Stenosis	Distal	Proximal	Stenosis	Distal
Coronal	1.0	4.9 ± 1.1	−15.0 ± 12.7	9.5 ± 6.2	−11.0 ± 2.1	−20.9 ± 14.4	−18.8 ± 16.7
	1.6	2.1 ± 0.9	−12.1 ± 14.7	9.6 ± 2.3	−11.5 ± 0.9	−18.0 ± 27.7	−7.9 ± 12.3
	3.0	10.0 ± 0.9	−3.1 ± 36.9	10.2 ± 4.0	4.4 ± 1.5	−17.2 ± 49.6	−15.6 ± 21.6
Axial	1.6	1.3 ± 1.2	−11.3 ± 8.7	−2.5 ± 2.6	0.5 ± 2.3	−9.6 ± 13.3	3.6 ± 4.6
	3.0	−7.5 ± 3.3	−35.3 ± 28.0	−0.0 ± 5.8	0.3 ± 2.6	−24.3 ± 26.5	−6.4 ± 3.1

The flow region of interest was divided into three regions with respect to the stenosis, proximal (z < −22 mm), stenosis (−22 mm < z < 22 mm) and distal (22 mm < z)

coordinate system [16]. The Reynolds numbers (Re) at the inlet were Re = ρUD/ν = 3,500 and 1,380 for the 75 % and 90 % stenoses, respectively, where ρ = 1060 kg/m^3 was the blood density, U was the mean velocity at the inlet, D was the inlet internal diameter (22 mm) and the kinematic viscosity of blood was fixed as ν = 0.004 kg/m · s (Newtonian fluid). At the most stenosed point, Re increased to 7,000 and 4,363 for the 75 % and 90 % stenoses, respectively. The size of the computational domain was 0 ≤ r/D < 0.5, 0 ≤ θ < 2π, and −1.8 < z/D < 45 in the radial (r), azimuthal (θ) and axial (z) directions, respectively. The stenosis is positioned at z = 0. The outflow boundary was extended to avoid flow instability at the exit. At the inlet, the velocity profile was given as the time-averaged data calculated from 2D MR images. The convective boundary conditions were imposed at the outlet, and no-slip boundary conditions were applied at the phantom wall. The number of grid points were 240 × 120 × 672 in the r, θ and z directions, respectively, and the mesh density in the z direction was higher near the stenosis region with uniform distribution in the r and θ directions. The smallest mesh volume was approximately 3.48 × 10^{-5} mm^3. The solution was advanced with a time step that was determined through the condition of a Courant-Friedrichs-Lewy number < 1. The simulations were conducted over 400,000 time steps and finished after the statistical convergence.

Statistics

The flow rate and peak velocity of 4D and 2D flow MRI were time-averaged at each probe position and their temporal standard deviations were calculated (Figs. 2 and 3). The percent error of the flow rate was calculated based on the time-averaged value of flowmeter (Table 2) and was expressed as mean ± standard deviation. Subsequently, the time-averaged flow rates were analysed by partitioning the flow region of interest into three regions with respect to the stenosis: proximal (z < −22 mm), stenosis (−22 mm < z < 22 mm) and distal (22 mm < z). The peak velocity of CFD analysis was calculated at each axial position in the computational domain (Fig. 3),

and the peak velocities of 4D flow MRI and CFD were compared in the field of view (FOV) of 4D flow MRI (Table 3). A paired t-test was conducted to examine the differences between the results at the probe positions of 2D flow MRI and at the same positions of 4D flow MRI and to compare the results of 4D flow MRI performed using different acquisition parameters. Normality was tested with the Shapiro-Wilk W-test (p < 0.05). For the statistical analysis of flow fields (Fig. 4), linear regression analysis was used after the flow field of CFD analysis was reconstructed with the same resolution as 4D flow MRI acquisition. The root-mean-square of axial velocity fluctuation (u'_{rms}) is defined as:

$$u'_{rms} = \sqrt{\frac{1}{N}\sum_{i=1}^{N}\left(u_i - \bar{u}\right)^2},$$

where N is the number of time frames, and u_i and $\bar{u}$ are the instantaneous and time-averaged axial velocities based on Reynolds decomposition (Fig. 5). A p-value < 0.05 was considered to indicate statistical significance. Statistical analyses were performed using MedCalc software (MedCalc Software, Mariakerke, Belgium).

Results

Accuracy of the MRI flow rate—comparison with flowmeter

Figure 2 shows the distribution of the flow rate calculated from 4D flow MRI with a 1.6-mm isotropic resolution using an axial scan direction. The flow rate closely followed the output value of the flowmeter in the proximal and distal regions for 75 % stenosis. For 90 % stenosis, the flow rate measurement also exhibited a small percent error in those regions, namely, 0.5 % ± 2.3 % and 3.6 % ± 4.6 % in the proximal and distal regions, respectively. On the other hand, in the stenosis region, 4D flow MRI considerably underestimated
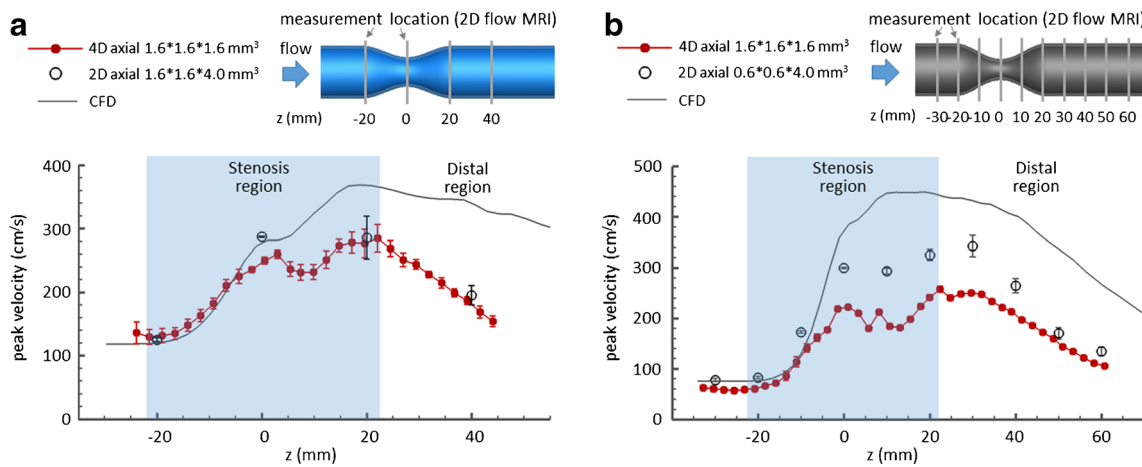
Fig. 3 Spatial variations in the time-averaged peak velocity measured with 4D flow magnetic resonance imaging (MRI) for (**a**) 75 % and (**b**) 90 % stenosis. The results of 2D flow MRI under the same flow conditions are also shown, and the corresponding imaging planes are illustrated in the top part of the image. A blue-shaded box denotes the stenosis region, and the error bar indicates the temporal standard deviation at each location. For 75 % stenosis, as a reference, the time-averaged peak velocity obtained from computational fluid dynamics (CFD) analysis is marked as a gray line in (a) and (b)

the flow rate with a W-shaped pattern, and the averaged error reached –11.3 % and –9.6 % for 75 % and 90 % stenoses, respectively. The mean error in the flow region of interest was –8.1 %±8.2 % and –2.7 %±11.3 % for 75 % and 90 % stenoses, respectively. When compared with the flow rates at the probe positions of 2D flow MRI, there was no significant difference between 4D and 2D flow MRI (2D vs. 4D: –1.9 %±11.7 % vs. –6.6 %±8.1 % for 75 % stenosis, $p=0.428$; –5.4 %±6.0 % vs. –3.2 %±5.0 for 90 % stenosis, $p=0.652$).

The effects of the acquisition parameters on the flow-rate measurement are summarised in Table 2. In the proximal region, 4D flow MRI showed small percent errors in flow rate with all combinations of scan parameters, and the maximum error was –11.5 %. In the stenosis region, the flow rates were underestimated by up to 35.3 % and their modulations increased with an increasing voxel size in the same scan

direction up to 49.6 %. In the distal region, spatial variations in the flow rate were quite reduced, resulting in a percent error of from –18.8 % to 10.2 %. With the same spatial resolution, an axial scan perpendicular to the flow direction showed lower percent errors than a coronal scan ($p < 0.001$).

Analysis of MRI peak velocity – comparison with computational fluid dynamics (CFD)

Figure 3 shows the spatial variations in the time-averaged peak velocity measured with 4D flow MRI. With the same in-plane resolution (Fig. 3a), 4D and 2D flow MRI provided almost identical peak velocity, except at the most stenotic point ($z=0$). Meanwhile, for 90 % stenosis (Fig. 3b), 2D flow MRI with finer resolution yielded a higher peak velocity in all regions ($p=0.001$). As shown in Table 3, the spatial resolution had a dominant effect on estimation of the peak velocity.

Table 3 Accuracy and precision of the peak velocity measured by 4D flow magnetic resonance imaging (MRI) according to scan direction, spatial resolution and velocity-encoding range

Scan direction	Spatial resolution, mm	Peak velocity, cm/s	
		75 % stenosis (velocity-encoding range = 350 cm/s)	90 % stenosis (velocity-encoding range = 400 cm/s)
4D Coronal	1.0	212.1 ± 77.8	178.4 ± 101.0
	1.6	199.6 ± 81.5	150.9 ± 86.6
	3.0	185.2 ± 75.5	108.0 ± 65.9
4D Axial	1.6	208.9 ± 66.0	161.6 ± 70.8
	3.0	199.0 ± 85.7	137.7 ± 67.7
2D Axial	1.6 (75 % stenosis)	223.2 ± 78.2	216.3 ± 100.4
	0.6 (90 % stenosis)		
CFD		274.6 ± 92.8	295.1 ± 148.1

Large standard deviations of the peak velocity are caused by the changes of flow patterns across the stenosis, as shown in Fig. 5
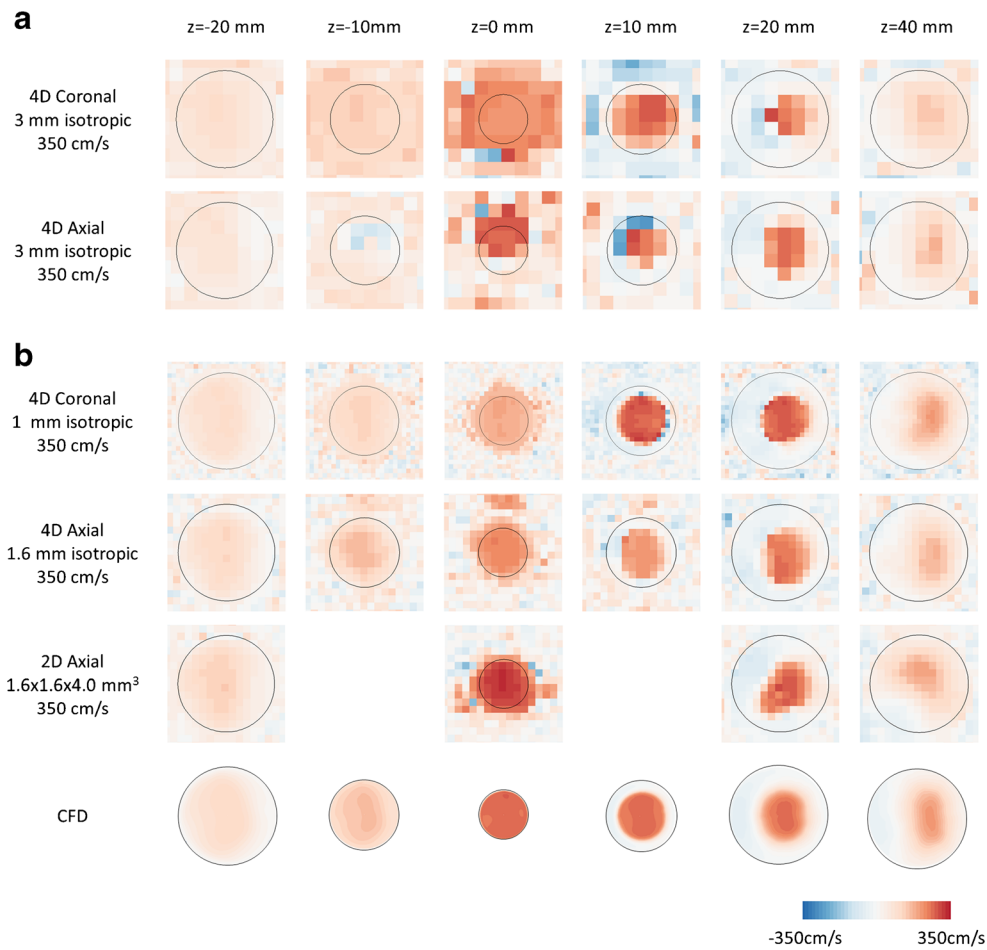
Fig. 4 Contours of the time-averaged axial velocity for 75 % stenosis at the axial planes of the phantom with (**a**) 3-mm and (**b**) 1-mm and 1.6-mm isotropic resolutions. The axial positions and the acquisition parameters are indicated in the top row and the left column, respectively. The black line denotes the phantom wall. Linear interpolation is applied to obtain the velocity field between the magnetic resonance image planes. Contours of the time-averaged axial velocity for 90 % stenosis at the axial planes of the phantom with (**c**) 3-mm and (**d**) 1-mm and 1.6-mm isotropic resolutions

Overall, the peak velocity from 4D and 2D flow MRI was underestimated compared with that of higher-resolution CFD analysis. The underestimation rates of 4D flow MRI were more than 22.8 % for 75 % stenosis and more than 39.5 % for 90 % stenosis.

Analysis of MRI flow patterns – comparison with CFD

To investigate the flow patterns of 4D flow MRI, the velocity fields at axial positions were compared with those of CFD analysis. Fig. 4a and c show the time-averaged axial velocity with 3-mm isotropic resolution, which allows a scan within a clinically feasible amount of time (<10 min) in coronal and axial scanning orientations. The given voxel size was too large to resolve the in-plane variations in the axial velocity, particularly the thin layer of the recirculating zone in the stenosis region (z = 10 mm). Also, near the narrowest point (z = 0), partial volume effects of the PC-MRI were prominent outside the flow phantom boundary (coronal) or high-velocity

components were dislocated (axial). On the distal side of the stenosis, some negative velocity components in the vicinity of the turbulent jet were detected, which caused underestimation of the flow rate and peak velocity. On the other hand, with 1-mm or 1.6-mm isotropic resolution, the time-averaged axial velocity was in good agreement with that of CFD analysis (Fig. 4b and d). At z ≥ 10 mm, the flow characteristics of the post-stenotic jet, such as reverse flows (recirculation bubble) and flow eccentricity, were well captured. In particular, the velocity distribution of the post-stenotic jet at z = 10 mm with 1-mm isotropic resolution was almost identical to that of CFD analysis ($R^2 = 0.851$ and 0.733 for 75 % and 90 % stenoses, respectively, $p < 0.001$). On the proximal side of the stenosis, the partial volume effect was minimised, and the velocity profiles were well appreciated with 4D flow MRI.

The development of the post-stenotic jet and the recirculating flow showed a high similarity between 4D flow MRI with 1-mm isotropic resolution and CFD analysis, as shown in Fig. 5a and c. The maximum thickness of the
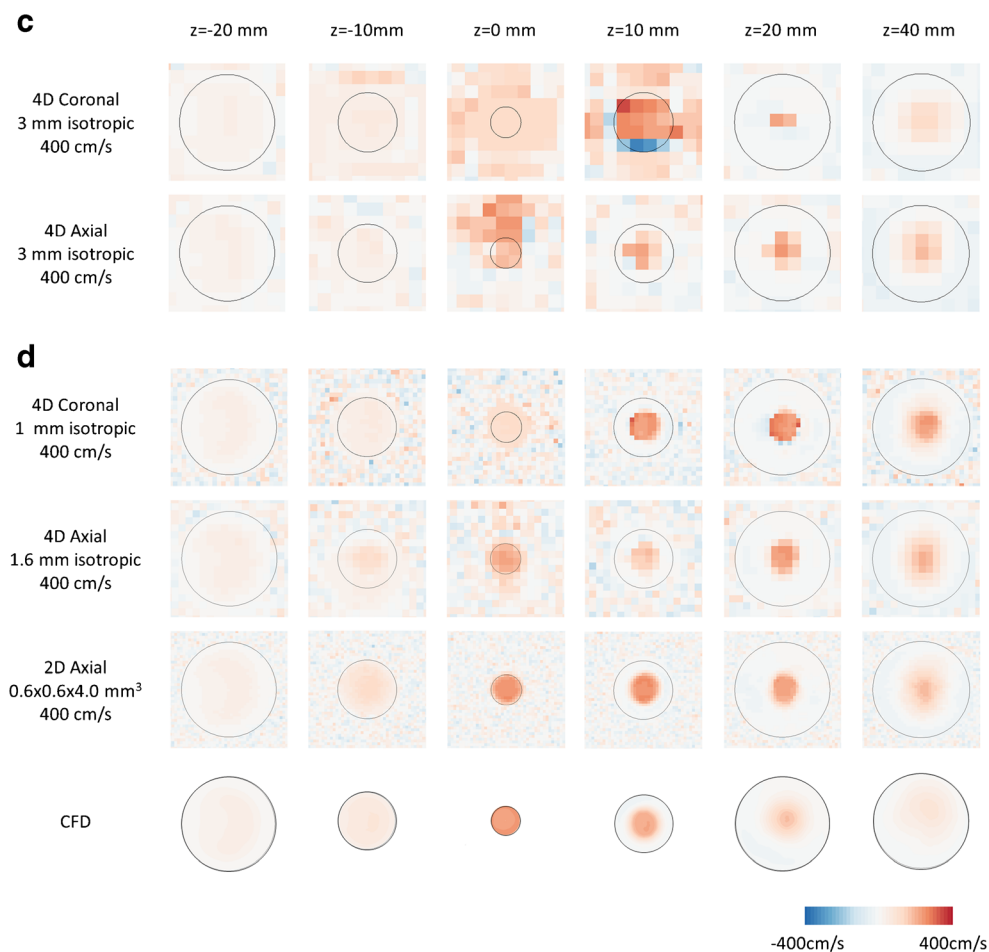
Fig. 4 (continued)

reverse-flow region (t_r in Fig. 5a and c) was estimated within a 1-mm difference (4D flow MRI vs. CFD: 6 mm vs. 5.8 mm for 75 % stenosis; 5 mm vs. 4.1 mm for 90 % stenosis). However, the length of the recirculation bubble (d_r in Fig. 5a and c) was underestimated by 34.3 % and 22.7 % for 75 % and 90 % stenoses, respectively, because the flow measurement in low-velocity regions near the wall was susceptible to noise. Also, even with 1-mm isotropic resolution, direct interpretation of the flow information acquired from 4D flow MRI was limited in turbulent flow characteristics because the voxel-averaged velocity of 4D flow MRI failed to capture flow structures smaller than the voxel size. As shown in Fig. 5b and d, the region of large velocity fluctuations mostly disappeared on the distal side of the stenosis. With 3-mm isotropic resolution, although the rough profile of post-stenotic jet was obtained, the interpretation of reverse flow and velocity fluctuations was limited. Figure 6 shows snapshots of the streamlines around the stenotic region for 75 % stenosis (see Supplementary Movies 1 [Fig. 6a] and 2 [Fig. 6b]). With 1.6-mm isotropic resolution, the recirculation flow was captured on the distal side of the stenosis and the centre of the vortex was clearly identified. With 3-mm isotropic resolution, the vortex

outlines were mostly untraceable and the streamlines were disconnected at several locations.

Discussion

The major findings of our present study are as follows: (a) 4D flow MRI accurately measured the flow rate in proximal and distal regions of the stenosis in axial scan direction; (b) the peak velocity of post-stenotic flow was considerably underestimated with 4D flow MRI; (c) with 1-mm or 1.6-mm isotropic resolution, 4D flow MRI demonstrated the principal characteristics of the post-stenotic jet such as recirculating flow; and (d) 4D flow MRI had a limitation in the direct calculation of the turbulent velocity fluctuation.

In the stenosis region, the flow rate measured was less accurate than that in the other regions and the first source of error was the flow acceleration [17]. The derivation of phase contrast imaging based on a first-order approximation produces errors that are proportional to the amount of local acceleration and the time difference between the
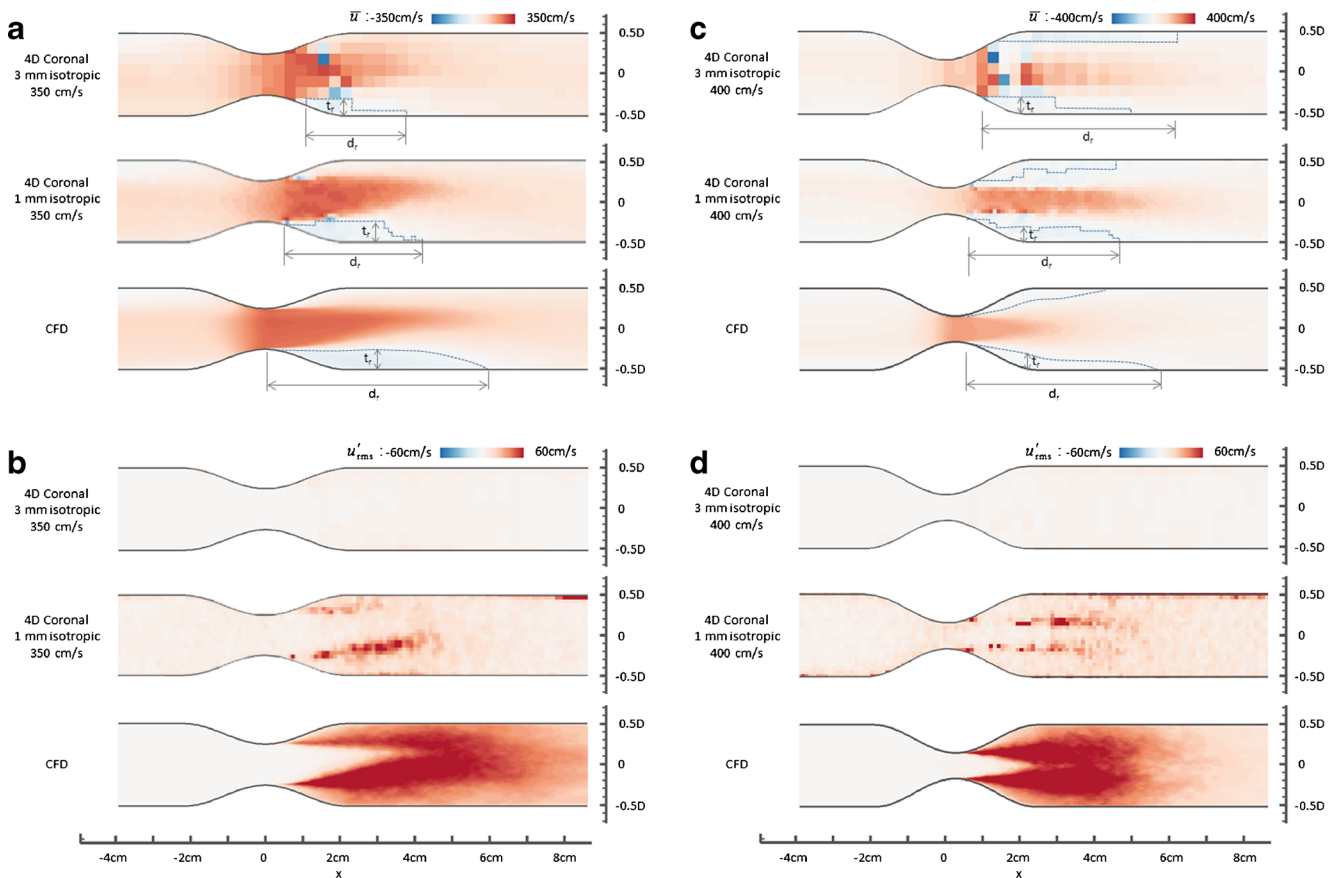
Fig. 5 Contours of the time-averaged axial velocity ($\bar{u}$; upper panel) and the root-mean-square of axial velocity fluctuation (u'_{rms}; lower panel) obtained from 4D flow magnetic resonance imaging (MRI) and computational fluid dynamics (CFD) analysis. Left and right columns correspond to 75 % and 90 % stenoses, respectively. The acquisition parameters are indicated in the left column. In (**a**), the dashed lines denote zero axial velocity, and t_r and d_r indicate the thickness of the reverse flow and the length of the recirculation bubble, respectively

moment centre of the velocity-encoding gradients and the centre of the echo [18]. In the distal region of stenosis, as the flow evolves across the stenosis, the quality of the velocity field measurement relied on whether 4D flow MRI was able to resolve the post-stenotic jet and the reverse flow. With 3-mm isotropic resolution, the intravoxel dephasing [19] and the signal loss due to the velocity fluctuations in a voxel caused accuracy degradation in high-velocity regions. Consequently, large modulations of the flow rate (Table 2) seriously compromised the reliability of flow rate measurement in the stenosis region, regardless of the accuracy of the averaged flow rate.

To evaluate the stenosis severity, one of the important parameters is the peak velocity, which is directly related to the pressure gradient. Although much effort has been made to accurately measure the peak velocity using MRI, it has been reported that the peak velocity from MRI was underestimated compared with Doppler evaluation [9, 10] and particle image velocimetry [11]. Likewise, in the present study, flow MRI did not capture the traces of the peak velocity predicted by CFD analysis, and the discrepancy rapidly grew downstream of the stenosis (Fig. 3). Increasing the spatial resolution improved

the estimation of the peak velocity, as shown in Table 3, but 1-mm isotropic resolution also showed large discrepancies. The complex flow patterns that contained small-scale structures (i.e., vortices), which had difficulty dealing with the voxel size of MRI (Fig. 4), hampered the peak velocity estimation. In stenotic flows, selection of a minimal echo time could improve the estimation of the peak velocity, as reported for 2D flow MRI [20] and 4D flow MRI [21].

Four-dimensional flow MRI has insufficient temporal and spatial resolution to capture small-scale structures of post-stenotic turbulent characteristics at a high Reynolds number [18]. In our present study, 4D flow MRI provided only a rough image of the turbulent velocity fluctuations (Fig. 5b and d). For 75 % stenosis, the magnitude of the turbulent velocity fluctuations was much smaller in its maximum (–33.1 %) and averaged (–64.8 %) values with 1-mm isotropic resolution. To complement the limitation of 4D flow MRI for predicting turbulent characteristics, various methods have been introduced using multipoint velocity encoding [22, 23]. Despite a prolonged scanning time, turbulent terms such as turbulent kinetic energy have been shown to be accurately predicted using these methods.

Fig. 6 Snapshots of the streamlines around the stenosed region for 75 % stenosis: (**a**) axial scanning with 1.6-mm isotropic resolution and (**b**) coronal scanning with 3-mm isotropic resolution
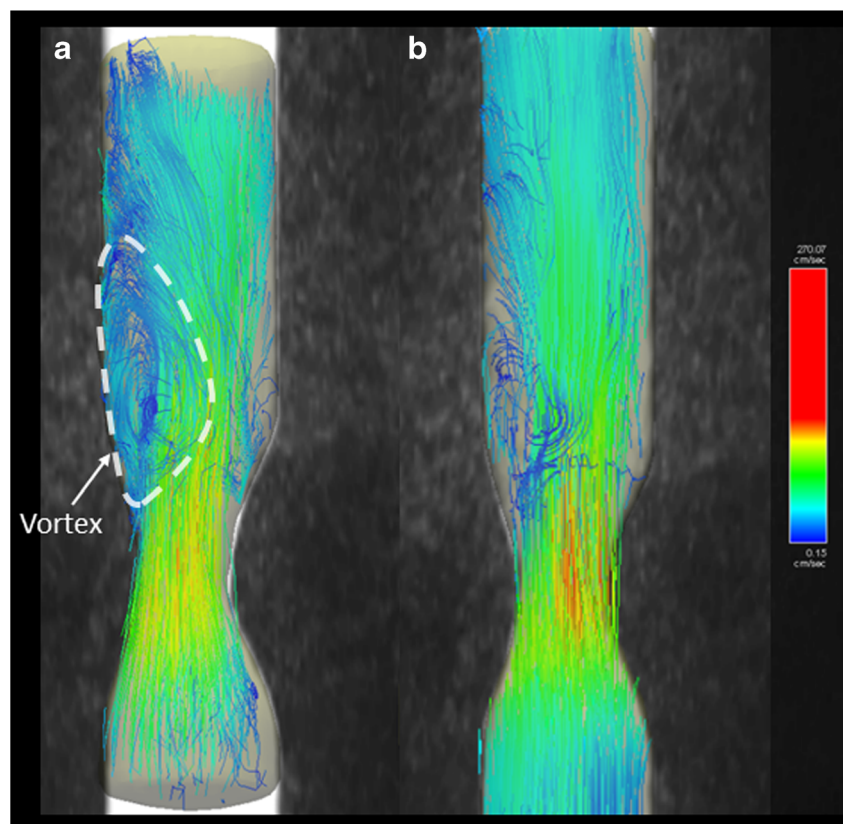
Fine spatial resolution was helpful for capturing the principal characteristics of post-stenotic jets [2, 24]. In the present study, with 1-mm or 1.6-mm isotropic resolution, the flow characteristics were well captured and the intravoxel dephasing was limited to very narrow regions (Fig. 5). However, 1-mm isotropic resolution did not provide better flow-rate measurements than 1.6-mm isotropic resolution (Table 2). In 3D PC-MRI, the signal-to-noise ratio (SNR) was proportional to the square root of the voxel volume with a given FOV. SNR reduction with 1-mm isotropic resolution caused unrealistic velocity peaks in low-velocity regions and, consequently, the standard deviation of the flow rate was larger in the proximal and distal regions of the stenosis. In addition, with 1-mm isotropic resolution, the scan time increased to about 17 min (Table 1), which might hinder the widespread adoption of 4D flow MRI in clinical practice. Although a higher resolution may give better estimations of the peak velocity and flow field, considering the SNR reduction, refining the spatial resolution below 1 mm would not be necessary for flow-rate measurement under the present conditions.

The number of image slices in coronal scans was almost half or less of that in axial scans, and therefore coronal scanning required less time for the acquisition of 4D flow MRI than axial scanning (Table 1). With 1.6-mm isotropic resolution for 75 % stenosis, the coronal scanning was finished in 468 s, which was 36 % of the time required for axial scanning.

However, coronal scanning suffered from the partial volume effect (Fig. 4), leading to lower accuracy in the flow-rate measurement, because the scan orientation was not perpendicular to the flow direction [12]. Regarding the scan time requirement, recent advances allow 4D flow MRI acquisition within a single breath-hold [25] and these efforts will lead to widespread application of 4D flow MRI in the clinical setting.

In conclusion, 4D flow MRI accurately measured the flow rate in proximal and distal regions of the stenosis in axial scan direction and demonstrate the principal pattern of post-stenotic jets with 1-mm or 1.6-mm isotropic resolution. For application in the clinical situation, the limitations of 4D flow MRI in the estimations of peak velocity and turbulent characteristics, together with the scan time, should be overcome.

review board approval and informed consent were not required. Methodology: experimental, performed at one institution.

References

1. Hope TA, Markl M, Wigström L, Alley MT, Miller DC, Herfkens RJ (2007) Comparison of flow patterns in ascending aortic aneurysms and volunteers using four-dimensional magnetic resonance velocity mapping. J Magn Reson Imaging 26:1471–1479

2. Markl M, Kilner PJ, Ebbers T (2011) Comprehensive 4D velocity mapping of the heart and great vessels by cardiovascular magnetic resonance. J Cardiovasc Magn Reson 13:1–22

3. Reiter G, Reiter U, Kovacs G et al (2008) Magnetic resonance–derived 3-dimensional blood flow patterns in the main pulmonary artery as a marker of pulmonary hypertension and a measure of elevated mean pulmonary arterial pressure. Circ: Cardiovasc Imaging 1:23–30

4. Bächler P, Pinochet N, Sotelo J et al (2013) Assessment of normal flow patterns in the pulmonary circulation by using 4D magnetic resonance velocity mapping. Magn Reson Imaging 31:178–188

5. Geiger J, Hirtler D, Burk J et al (2014) Postoperative pulmonary and aortic 3D haemodynamics in patients after repair of transposition of the great arteries. Eur Radiol 24:200–208

6. Harloff A, Albrecht F, Spreer J et al (2009) 3D blood flow characteristics in the carotid artery bifurcation assessed by flow-sensitive 4D MRI at 3T. Magn Reson Med 61:65–74

7. van der Hulst AE, Westenberg JJ, Kroft LJ et al (2010) Tetralogy of fallot: 3D velocity-encoded MR imaging for evaluation of right ventricular valve flow and diastolic function in patients after correction 1. Radiology 256:724–734

8. Markl M, Chan FP, Alley MT et al (2003) Time-resolved three-dimensional phase-contrast MRI. J Magn Reson Imaging 17:499–506

9. Kilner PJ, Manzara CC, Mohiaddin RH et al (1993) Magnetic resonance jet velocity mapping in mitral and aortic valve stenosis. Circulation 87:1239–1248

10. Caruthers SD, Lin SJ, Brown P et al (2003) Practical value of cardiac magnetic resonance imaging for clinical quantification of aortic valve stenosis comparison with echocardiography. Circulation 108:2236–2243

11. Khodarahmi I, Shakeri M, Kotys-Traughber M, Fischer S, Sharp MK, Amini AA (2014) In vitro validation of flow measurement with phase contrast MRI at 3 tesla using stereoscopic particle image velocimetry and stereoscopic particle image velocimetry-based computational fluid dynamics. J Magn Reson Imaging 39:1477–1485

12. Tang C, Blatter DD, Parker DL (1993) Accuracy of phase-contrast flow measurements in the presence of partial-volume effects. J Magn Reson Imaging 3:377–385

13. Stalder A, Russe M, Frydrychowicz A, Bock J, Hennig J, Markl M (2008) Quantitative 2D and 3D phase contrast MRI: optimized analysis of blood flow and vessel wall parameters. Magn Reson Med 60:1218–1231

14. Sherwin S, Blackburn HM (2005) Three-dimensional instabilities and transition of steady and pulsatile axisymmetric stenotic flows. J Fluid Mech 533:297–327

15. Vreman A (2004) An eddy-viscosity subgrid-scale model for turbulent shear flow: algebraic theory and applications. Phys Fluids (1994-present) 16:3670–3681

16. Kim J, Kim D, Choi H (2001) An immersed-boundary finite-volume method for simulations of flow in complex geometries. J Comput Phys 171:132–150

17. Ståhlberg F, Søndergaard L, Thomsen C, Henriksen O (1992) Quantification of complex flow using MR phase imaging—a study of parameters influencing the phase/velocity relation. Magn Reson Imaging 10:13–23

18. Elkins CJ, Alley MT (2007) Magnetic resonance velocimetry: applications of magnetic resonance imaging in the measurement of fluid motion. Exp Fluids 43:823–858

19. Oshinski JN, Ku DN, Pettigrew RI (1995) Turbulent fluctuation velocity: the most significant determinant of signal loss in stenotic vessels. Magn Reson Med 33:193–199

20. O'Brien KR, Cowan BR, Jain M, Stewart RA, Kerr AJ, Young AA (2008) MRI phase contrast velocity and flow errors in turbulent stenotic jets. J Magn Reson Imaging 28:210–218

21. Kadbi M, Negahdar M, Traughber M, Martin P, Stoddard MF, Amini AA (2014) 4D UTE flow: a phase-contrast MRI technique for assessment and visualization of stenotic flows., Magnetic Resonance in Medicine

22. Dyverfeldt P, Sigfridsson A, Kvitting JPE, Ebbers T (2006) Quantification of intravoxel velocity standard deviation and turbulence intensity by generalizing phase-contrast MRI. Magn Reson Med 56:850–858

23. Binter C, Knobloch V, Manka R, Sigfridsson A, Kozerke S (2013) Bayesian multipoint velocity encoding for concurrent flow and turbulence mapping. Magn Reson Med 69:1337–1345

24. Hope MD, Hope TA, Meadows AK et al (2010) Bicuspid aortic valve: four-dimensional MR evaluation of ascending aortic systolic flow patterns 1. Radiology 255:53–61

25. Dyvorne H, Knight-Greenfield A, Jajamovich G et al (2014) Abdominal 4D flow MR imaging in a breath hold: combination of spiral sampling and dynamic compressed sensing for highly accelerated acquisition., Radiology